ACS APPLIED MATERIALS & INTERFACES

www.acsami.org Research Article

Role of the Metal–Semiconductor Interface in Halide Perovskite Devices for Radiation Photon Counting

Shreetu Shrestha, Hsinhan Tsai, Michael Yoho, Dibyajyoti Ghosh, Fangze Liu, Yusheng Lei, Jeremy Tisdale, Jon Baldwin, Sheng Xu, Amanda J. Neukirch, Sergei Tretiak, Duc Vo, and Wanyi Nie*

Cite This: *ACS Appl. Mater. Interfaces* 2020, 12, 45533–45540 Read Online

ACCESS | Metrics & More | Article Recommendations | Supporting Information

ABSTRACT: Halide perovskites are promising optoelectronic semiconductors. For applications in solid-state detectors that operate in low photon flux counting mode, blocking interfaces are essential to minimize the dark current noise. Here, we investigate the interface between methylammonium lead tri-iodide ($MAPbI_3$) single crystals and commonly used high and low work function metals to achieve photon counting capabilities in a solid-state detector. Using scanning photocurrent microscopy, we observe a large Schottky barrier at the $MAPbI_3$/Pb interface, which efficiently blocks dark current. Moreover, the shape of the photocurrent profile indicates that the $MAPbI_3$ single-crystal surface has a deep fermi level close to that of Au. Rationalized by first-principle calculations, we attribute this observation to the defects due to excess iodine on the surface underpinning emergence of deep band-edge states. The photocurrent decay profile yields a charge carrier diffusion length of 10–25 μm. Using this knowledge, we demonstrate a single-crystal $MAPbI_3$ detector that can count single γ-ray photons by producing sharp electrical pulses with a fast rise time of <2 μs. Our study indicates that the interface plays a crucial role in solid-state detectors operating in photon counting mode.

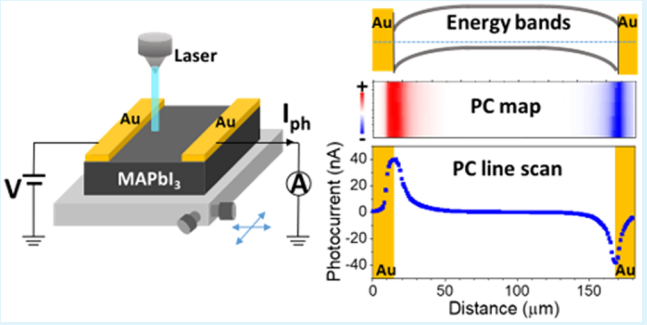

KEYWORDS: *perovskite, scanning photocurrent microscopy, metal–semiconductor interface, Schottky junction, solid-state detector*

INTRODUCTION

Halide perovskites are excellent semiconductors for optoelectronic applications such as photovoltaics,[1,2] light-emitting diodes,[3,4] lasers,[5,6] photodetectors,[7−18] and ionizing radiation detectors.[19−27] Over a short period of time, halide perovskite single-junction solar cells have reached power conversion efficiencies above 25%,[28] approaching amorphous silicon devices.

To further improve device performance, it is essential to understand the interface between perovskite and subsequent device layers. Interfaces are especially critical in low photon flux applications like γ-ray detectors, which typically operate in single-photon counting mode (i.e., each individual γ-ray photon interaction is measured as an electrical pulse). Accurately counting the number and measuring the amplitude of γ-ray-induced electrical pulses is the first step towards energy-resolved γ-ray spectroscopy. Since small electrical pulses can be easily suppressed by background noise, the acceptable noise level is much lower for γ-ray detectors than solar cells that operate at higher photon flux. Leakage current or dark current is a major source of noise, and blocking contacts are often used to minimize the dark current. Using asymmetric Schottky barrier contacts in $MAPbI_3$ single-crystal devices, He et al. suppressed the dark current and obtained 10% resolution at 122 keV.[23] However, the exact nature of the barrier and energy band bending at the metal–perovskite interface, which is essential for efficient γ-ray detector design, is not fully understood.

To analyze the interfaces in perovskite devices, techniques such as photoemission spectroscopy[29−31] and Kelvin probe force microscopy[30,32] have been used. Here, we present an in-depth study of interfaces between single-crystal methylammonium lead iodide ($MAPbI_3$) and low (Pb) and high (Au) work function metal contacts using scanning photocurrent microscopy (SPCM). SPCM is a nondestructive method used to probe the local energy band bending and transport properties across interfaces, which has been successfully applied to various materials such as semiconductor nanowires,[33−38] two-dimensional (2D) materials,[39] quantum dot thin films,[40] and also perovskites.[41−44] In this technique, a laser is scanned across the surface of a lateral device and photocurrent as a

Received: June 29, 2020
Accepted: September 4, 2020
Published: September 4, 2020

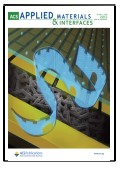

https://dx.doi.org/10.1021/acsami.0c11805
ACS Appl. Mater. Interfaces 2020, 12, 45533–45540

function of the laser position is measured to obtain a spatially resolved photocurrent map. It provides information about local energy band bending, charge transport, and recombination (provided that the laser intensity is kept low enough so that the locally photoexcited charge does not disturb the interfacial electric field). Typically, if a Schottky barrier exists at a metal/semiconductor interface, the band bending direction (upward or downward) and the barrier height will determine the polarity and magnitude of the local photocurrent extracted, respectively. Moreover, carrier diffusion length can also be estimated from the photocurrent decay if at least one of the interfaces forms a Schottky barrier with the semiconductor.

By analyzing the shape of photocurrent profiles obtained from SPCM measurements, we find that the energy band at the $MAPbI_3$/metal interface bends downwards for both Pb and Au contacts. This indicates that the surface of the perovskite single crystal has a deeper Fermi level than Pb's work function and is close to that of Au. The appearance of these deep band-edge states is further rationalized by quantum-chemical calculations suggesting that the p-type doping emerges due to the excess iodine defects on the surface. Moreover, we show that perovskite's band edge energies depend on the specific surface chemical composition; for instance, PbI_2 termination being commensurate with our synthetic protocol. Although the energy bands bend downward for both Pb and Au contacts, we find that the barrier height at the Au contact is much lower, resulting in Ohmic-like current−voltage characteristics. Utilizing the decay of the photocurrent profiles at the perovskite/metal interface, we further extract carrier diffusion length in $MAPbI_3$ to be in the range of 10−25 μm. Finally, using Au and Pb contacts, we fabricate vertical $MAPbI_3$ single-crystal devices. Owing to the large barrier height at the $MAPbI_3$/Pb interface, we are able to reduce the dark current to 280 nA/cm^2 at a field of 700 V/cm (reverse bias) while efficiently extracting the γ-ray-induced charge carriers with fast rise times of <2 μs at room temperature.

RESULTS AND DISCUSSION

We start by comparing two commonly used halide perovskite single crystals, $MAPbI_3$ and $MAPbBr_3$ made into vertical devices with an Au/perovskite/Au structure and test their response under γ-ray photons. Figure 1a compares the normalized photocurrent pulse response to a ^{137}Cs source from the $MAPbI_3$ and $MAPbBr_3$ detectors. A typical pulse from a commercial Cadmium Zinc Telluride (CZT) detector measured under the same conditions is also plotted as a reference in Figure 1a. The plot shows that the pulse shape of $MAPbI_3$ is comparable to the CZT reference with a fast rise time of 7 μs. However, the rise time of the $MAPbBr_3$ detector is much slower. The rise time statistics over 24 pulses is plotted as a histogram in Figure 1b, which shows that the rise time of $MAPbI_3$ has a mean value of 5 ± 3 μs. In a sharp contrast, those of $MAPbBr_3$ have a wider spread with a much larger average value of approximately 31 ± 13 μs. The mobility of $MAPbBr_3$ is, on average, lower than $MAPbI_3$, which could explain the slower rise time.[45] Moreover, although $MAPbBr_3$ has a higher band gap than $MAPbI_3$, in our previous report, we found that $MAPbBr_3$ has electronic impurity that can inject electron at room temperature resulting in a higher dark current.[26]

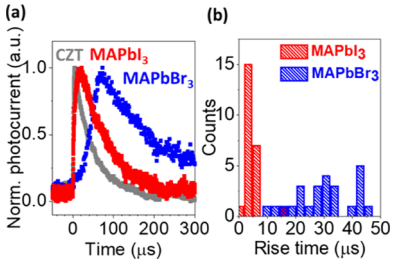

Figure 1. γ-ray-induced pulse response. (a) Normalized γ-ray-induced photocurrent pulses under a ^{137}Cs (661.7 keV) source at room temperature from the CZT reference (gray), $MAPbBr_3$ (blue), and $MAPbI_3$ (red) detectors with gold contacts at 50 V bias taken at room temperature. (b) Statistical distribution of pulse rise time for $MAPbI_3$ and $MAPbBr_3$ detectors when operated under the same conditions.

The promising results of sharp pulses in Figure 1a thus motivate an in-depth investigation of the effect of metal contacts to optimize $MAPbI_3$ single-crystal devices. We fabricate lateral $MAPbI_3$ single-crystal devices with (1) Pb−Pb, (2) Au−Au, and (3) Au−Pb contacts (Figure S1) and measure the dark current−voltage characteristics of the devices as shown in Figure 2b. The S-shaped curve for Pb−Pb contacts (blue) indicates the presence of a double Schottky barrier at the two Pb/$MAPbI_3$ interfaces, while the nearly linear curve for Au−Au contacts (red) indicates that there is an ohmic contact with small or no Schottky barrier at the Au/$MAPbI_3$ interfaces. Hence, the devices with asymmetric Au−Pb contacts (black) with an ohmic-like Au and blocking Pb contacts show a rectifying behavior.

To probe the local energy band bending with different metal contacts, we investigate the metal/$MAPbI_3$ interface using the SPCM. A typical SPCM photocurrent map and corresponding photocurrent line scan for a lateral $MAPbI_3$ single-crystal device with Pb−Pb contacts and a channel width of ∼160 μm is shown in Figure 2c. (Note red and blue indicate maximum and minimum current, respectively.) The photocurrent maxima and minima appear near the metal contact edges, where charge collection is the most efficient. Locally photoexcited charge carriers diffuse in all directions. However, when the laser is close to the contacts, electrons can diffuse to the depletion region near the contact and be swiftly extracted by the interfacial built-in potential. Since Pb is a low work function metal ($W_{\text{F-Pb}}$ (−4.25 eV) > $E_{\text{F-MAPbI}_3}$), we anticipate a downward band bending at the interface, as shown in the inset of Figure 2c. The direction of the photocurrent peak is indeed consistent with the bands bending down toward Pb contacts. Since we are measuring current from source to drain, this results in a positive photocurrent peak near the source contact and a negative peak near the drain contact. Holes, on the other hand, will be blocked near this interface and recombine in the bulk. As the laser moves away from the contacts, fewer electrons will be collected, resulting in an exponential photocurrent decay.

For devices with Au−Au contacts, an upward band bending at the interface is expected ($W_{\text{F-metal}}$ (−5.1 eV) < $E_{\text{F-MAPbI}_3}$). This would result in a photocurrent profile with a negative (positive) peak at the source (drain) contact. In contrast, the measured line scans have a positive (negative) peak at the source (drain) contact (Figure 2d), which is similar to what we obtained for devices with Pb−Pb contacts. This indicates that our $MAPbI_3$ crystals have a surface Fermi level deeper than the work function of Au. Notably, $MAPbI_3$ with p-type characteristics has also been observed in literature on both single

https://dx.doi.org/10.1021/acsami.0c11805
ACS Appl. Mater. Interfaces 2020, 12, 45533−45540

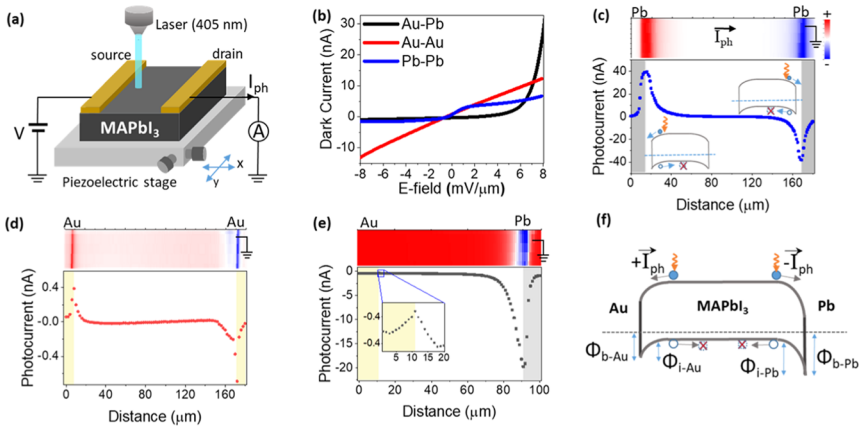

Figure 2. Scanning photocurrent microscopy. (a) Schematic of the experimental setup. For all measurements, bias voltage is applied to the source electrode on the left and the drain electrode on the right is grounded. (b) Dark current as a function of electric filed for $MAPbI_3$ single-crystal devices with Pb−Pb (blue), Au−Au (red), and Au−Pb (black) lateral contacts. Two-dimensional photocurrent map (top) and line scan (bottom) at 0 bias voltage (right electrode grounded) for $MAPbI_3$ single-crystal devices with (c) Pb−Pb, (d) Au−Au, and (e) Au−Pb electrodes (red and blue correspond to the maximum and minimum currents, respectively). (f) Schematic energy band diagram of Au/$MAPbI_3$/Pb. The barrier height and built-in potential at the Au/$MAPbI_3$ interface ($\Phi_{b\text{-}Au}$, $\Phi_{i\text{-}Au}$) are lower than that at the Pb/$MAPbI_3$ interface ($\Phi_{b\text{-}Pb}$, $\Phi_{i\text{-}Pb}$).

crystals and thin films, suggesting such surface doping is favorable in the $MAPbI_3$ system.[42,44,46,47]

Although the direction of the photocurrent profiles in devices with Pb−Pb and Au−Au contacts are similar, their magnitudes are vastly different. To compare directly the interface of $MAPbI_3$ with Au contacts to that with Pb contacts, we measure asymmetric devices with Au as the source contact and Pb as the drain contact. The SPCM maps of the Au−Pb device (Figure 2e) show a large negative photocurrent near the drain Pb contact. If we zoom in on the photocurrent line scan near the source (Au contact) (Figure 2e inset), we can see that a small positive photocurrent peak does exist and that the magnitude is comparable to that of the Au−Au device. However, the photocurrent peak near the drain (Pb electrode) is about two orders of magnitude higher. The built-in potential (Φ_i), which can be approximated as the difference between the $MAPbI_3$ Fermi level and metal work function ($\Phi_i = E_{F\text{-}MAPbI_3} - W_{F\text{-}metal}$), at the Pb/$MAPbI_3$ interface is larger than that at the Au/$MAPbI_3$ interface, as shown in Figure 2f. Hence, the locally photoexcited electrons can be more efficiently extracted resulting in a larger photocurrent peak. This larger band bending at the Pb/$MAPbI_3$ interface also leads to a higher barrier for holes, which explains the s-shaped current−voltage curve observed for Pb−Pb contacts in Figure 2b.

To understand the electronic properties of the $MAPbI_3$ surface at the atomistic level, we further perform first-principle-based computations. Details of the computational approach are provided in the Supporting Information. To construct a realistic computational model, we consider a slab of $MAPbI_3$ with two different types of terminations, methylammonium iodide (MAI) and PbI_2, for the (001) surface. Notably, (001) is also the surface used as electrical contacts in the experimental part and previous studies consistently indicated that it is the most stable surface for $MAPbI_3$.[48,49] However, the exact chemical composition of the terminating layer can vary depending on the synthesis conditions. Thus, we consider both MAI and PbI_2 terminations in this work. After complete relaxation of the internal coordinates of these $MAPbI_3$ slabs (Figure S2), we do not observe any considerable surface reconstructions, which is also supported by recent microscopy-based studies.[50,51]

In agreement with previous studies,[48,49] the electronic density of states (DOS) does not have any surface-localized mid-gap states for either termination type of the $MAPbI_3$ slabs considered (Figure S3). Importantly, band diagrams of $MAPbI_3$ plotted with respect to the vacuum level exhibit that the band edge positions strongly depend on the surface termination (Figure 3a). The PbI_2-terminated surface has deeper band edge states compared to that for the MAI-terminated one. Consequently, the valance band (VB) edge for the PbI_2-terminated surface is 5.56 eV whereas the MAI-terminated one has a VB edge of 4.88 eV. Such difference in the band edge positions is related to the variation of the effective surface dipole appearing due to distinct chemical composition. During the sample preparation, PbI_2-terminated surfaces could have been the energetically favored phase. Thus, $MAPbI_3$ with PbI_2 termination should feature deep band-edge states, matching with our current−voltage (Figure 1b), ultraviolet photoelectron spectroscopy (UPS, Figure S4), and X-ray photoelectron spectroscopy results (XPS, Figure S5).

Moreover, from our SPCM results we find downward band bending at the metal−semiconductor interface for both Au and Pb metals, indicating a surface Fermi level deeper than that of Au. To find the atomistic origin, we further investigate the defect properties of the perovskite surface. As previous studies demonstrated, defects with excess iodine on the surface (I_i) are energetically the easiest to form and thus we consider this defect as the dominant one in our samples (Figure S6).[52] We further investigate the effects of these defects on the electronic properties of $MAPbI_3$. The plotted projected density of states (pDOS) in Figure 3b shows that the I_i defect states are located between the valence and conduction bands, that is, mid-gap states arise with the introduction of this defect. More importantly, as shown in Figure 3b, the defect state appears just above the valence band maxima (~0.25 eV from VBM), a signature of p-type doping in a semiconductor. Furthermore, the charge density distribution of the defect state plotted in Figure 3c is strongly spatially localized, indicating the efficient carrier trapping ability of this defect state.[53] The charge density plot also reveals that the p-orbitals of the excess surface iodine are the dominant contribution to this p-type defect state. Details of charge densities of band-edge states are included in

https://dx.doi.org/10.1021/acsami.0c11805
ACS Appl. Mater. Interfaces 2020, 12, 45533−45540

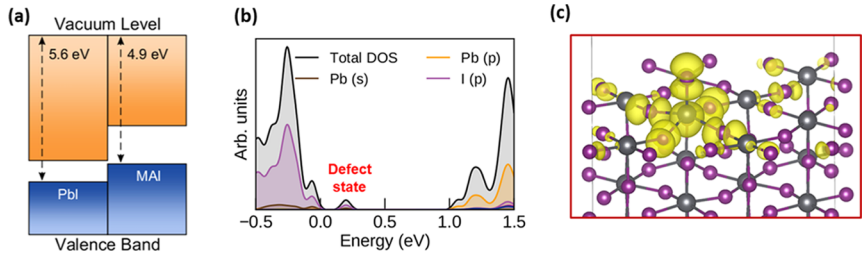

Figure 3. Surface energetics and electronic structure of $MAPbI_3$. (a) Energetically aligned valence band maxima and conduction band minima energies and work functions for $MAPbI_3$ with PbI_2 and MAI termination. (b) Projected density of states (pDOS) of $MAPbI_3$ with iodine interstitial defect on the surface. The p-type defect state appears near the valence band edge. (c) Charge density distribution corresponding to the iodine interstitial defect state. The charge density has been represented by yellow isosurface (density = 0.001 eV/Å^3). The gray and purple colored spheres are Pb and I atoms; MA molecules are not shown for clarity.

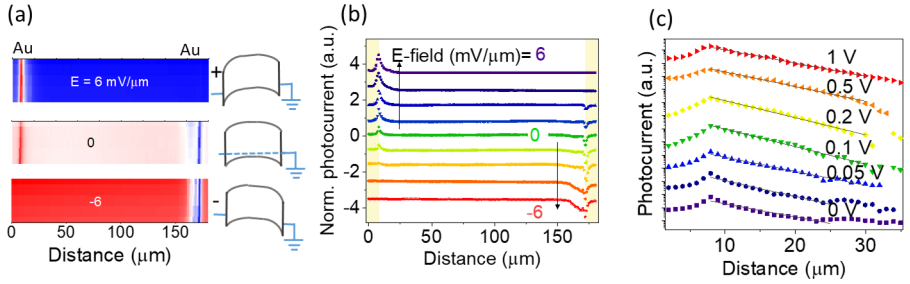

Figure 4. Electric field dependence. (a) SPCM maps at different electric fields (bias is on the source electrode (left), and drain electrode (right) is grounded) for $MAPbI_3$ single-crystal devices with Au−Au contacts (Red and blue correspond to maximum and minimum currents, respectively. Note the color scales are different). Schematic of the corresponding band bending with Au−Au contacts at different fields are shown on the left. (b) Linear and (c) semilog plot of line scans of photocurrent maps for devices with Au−Au contact.

the Supporting Information (SI) (Figure S7). Thus, our computational investigation indicates that easy-to-form[52] I_i defects can be the reason for the deep fermi level of the $MAPbI_3$ surface.

We performed further investigations of photocurrent profiles at different electric fields. At zero bias, band bending at the interface is due solely to the interface built-in potential (Φ_i) but when a voltage (V_a) is applied, the potential at the interface equals to $\Phi_i + V_a$. Figure 4a shows the electric field dependence of the photocurrent map for devices with Au−Au contacts. With a positive (negative) bias, the photocurrent peak near the source electrode increases (decreases) while the peak near the drain electrode decreases (increases). The normalized photocurrent line scan in Figure 4b clearly demonstrates this trend. (Absolute photocurrent magnitudes in SI Figure S8). The externally applied bias reinforces (diminishes) the interface built-in potential at the source (drain) resulting in an increase (decrease) in photocurrent peak as shown by the energy band schematic in Figure 4a. This behavior is consistent with previous reports on perovskite thin films[42] and Si nanowires.[33]

From the slope of the photocurrent decay profiles, we can obtain the minority carrier diffusion length (L) using the relation $I \propto \exp(-x/L)$, where x is the distance from the metal interface as explained in detail and modeled by Fu et al.[54] Briefly, the three main components that contribute to charge transport are (1) drift, (2) diffusion, and (3) thermoelectric effect. For low laser intensities, both thermoelectric effect and minority carrier drift can often be ignored. For Schottky contacts, the majority drift and diffusion cancel out and, therefore, the minority carrier diffusion dominates the photocurrent. The depletion region near the contacts for perovskites has been estimated to be ∼1 μm.[55] Since this is shorter than the photocurrent decay length, electron drift in the depletion region alone cannot account for the long photocurrent decay and consequently electron diffusion should be the limiting factor for the photocurrent profile.

We obtained electron diffusion lengths in the range of 10−25 μm, which is within the realm of values reported in literature.[46,56,57] Although there is some variation, an electric field dependence was not observed as shown in Figure 4c, which suggests a diffusion-limited transport in the system. Similar results have also been reported for perovskite thin films in this low electric field range.[42] At higher fields, drift could start playing a more dominant role in transport. Dynamic change in the built-in electric field attributed to ion migration in $MAPbI_3$ thin films at high field has also been studied with SPCM.[44]

From SPCM and current−voltage measurements, we find that due to the higher band bending at the Pb/$MAPbI_3$ interface, devices made by Pb/$MAPbI_3$/Au show a rectifying behavior. Utilizing this knowledge, next we fabricate vertical devices for γ-ray detection with a blocking Pb contact on one side and an Ohmic Au contact on the other side of a $MAPbI_3$ single crystal. Due to the rectifying nature of the Pb/$MAPbI_3$/Au device, the dark current in reverse bias is lower by more than an order of magnitude in comparison to that of the Au−Au devices, as shown in Figure 5a. For example, at a field of 260 V/cm, the Au−Pb devices have a dark current of 34 μA/cm^2, and at a reverse bias, the dark current dramatically reduces by 3 orders of magnitude to 84 nA/cm^2. Even at a higher reverse bias of 700 V/cm, the dark current is 280 nA/cm^2 and is stable for a few hours allowing for pulse counting for a longer time (Figure S9). As a result, the devices with Au−Pb contacts showed clean pulses in response to ^{241}Am, ^{133}Ba, and ^{137}Cs γ-ray sources at room temperature (Figure 5b). The

https://dx.doi.org/10.1021/acsami.0c11805
ACS Appl. Mater. Interfaces 2020, 12, 45533−45540

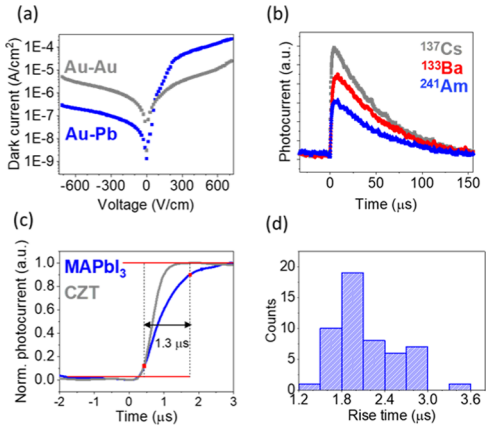

Figure 5. $MAPbI_3$ single-crystal γ-ray detector. (a) Dark current for devices with Au−Au (gray) and Au−Pb (blue) contacts. (b) γ-ray (^{241}Am, ^{133}Ba, and ^{137}Cs sources)-induced photocurrent pulse from the $MAPbI_3$ detector with Au−Pb contacts under room temperature and a 680 V/cm reverse bias. (c) Normalized pulse of a 2.2 mm thick $MAPbI_3$ device with Au−Pb contacts and a 5 mm thick CZT reference device (^{137}Cs source, 900 V/cm) and (d) rise time distribution histogram (^{137}Cs source, 900 V/cm).

baseline is clean and stable, which allows for resolving the low-energy γ-ray photon induced by a low-amplitude pulse signal from the ^{241}Am source. The rise time of the devices measured with our electronic setup was less than 2 μs (Figure 5c). This value is comparable to melt grown $CsPbBr_3$ devices reported in literature[24] and our CZT reference device measured under the same conditions.

CONCLUSIONS

In summary, this work has identified a promising material ($MAPbI_3$) as a γ-ray single-photon counter and provides guidelines for other solid-detector technologies operating under low photon flux condition. The high-quality $MAPbI_3$ crystals offer efficient single-photon counting with clean and sharp pulses that have rise times on par with commercial CZT detectors, which resolves problems in the $MAPbBr_3$ system with noisy and slow pulses. From our in-depth experiment and theory investigations, we find that it is crucial to understand both the nature of the perovskite's surface and the interface barriers when making contact with metals to design an efficient solid-state detector. By directly imaging the device using scanning photocurrent microscopy on the $MAPbI_3$ crystal, we observe a downward band bending when it is contacted by both Pb and Au, suggesting that the Fermi level at the $MAPbI_3$ single-crystal surface is deeper than Pb's work function and is close to that of Au. Such observation holds for both the single-crystal device and the thin-film device, consistent with literature, which is thus related to the nature of the $MAPbI_3$ surface grown from the solution. First-principle calculations of the perovskite surfaces suggest that iodine-rich conditions[52] near the surface lead to a stable PbI_2 surface termination, which significantly affects the work function of the material. Furthermore, the appearance of the deep band-edge states and p-doping are linked to the existence of iodine interstitial defects. From the photocurrent decay curves, we conclude that the $MAPbI_3$ electron diffusion lengths are in the range of 10−25 μm. We observe a large barrier at the $MAPbI_3$/Pb interface, which acts as a blocking contact. Subsequently, we demonstrate asymmetric devices with the Pb/$MAPbI_3$/Au diode structure, which efficiently blocks out the dark current and detects ^{241}Am, ^{133}Ba, and ^{137}Cs γ-ray sources at room temperature with rise times of a few microseconds.

Overall, our study reveals the importance of understanding the surface of the crystal and the interface barriers when making contact with metals. They play a key role when designing an efficient solid-state device using perovskite single crystals with clean baselines for low flux photon detections. Our work is thus meaningful for the design of next-generation γ-ray photon counter and also provides guidelines to new type of photon counting devices made with perovskite semiconductors.

EXPERIMENTAL METHODS

Single-Crystal Growth and Device Fabrication. $MAPbI_3$ single crystals were grown using the inverse temperature crystal growth method reported in literature.[58] Briefly, an equimolar ratio of methylammonium iodide (MAI) and lead iodide (PbI) is dissolved in γ butyrolactone (GBL) to obtain a 1 M solution. By heating 2 mL of this solution at 140 °C for a few hours, a small $MAPbI_3$ crystal (<1 mm) is obtained. These small crystals are further used as a seed and allowed to grow overnight in a fresh precursor solution to obtain large (~1 cm) $MAPbI_3$ single crystals. Finally, E-beam deposition (Au) or thermal deposition (Pb) is used to deposit 100 nm thick metal electrodes on (001) surface of $MAPbI_3$ crystals (Figure S1 in the SI). A wire mask is then used to define lateral channel width between a drain and a source metal electrode.

SPCM Measurements. A Kiethley 2400 is used to measure the dark and photocurrent. We always apply voltage bias on the source electrode and ground the drain electrode. For the SPCM measurements, devices are illuminated by a continuous 405 nm laser focused on the sample by a NA 0.5 50× objective lens. The diameter of the laser spot is approximately 1−2 μm as determined by our camera. Neutral density filters are used to reduce the laser intensity to 50−200 W/cm^2. Devices are mounted on a piezo-electric stage (Nano-Drive, MCL Inc.) and are moved in 1 μm increments from source to drain. Photocurrent as a function of laser position is recorded to obtain a photocurrent map. A schematic of the experimental setup is shown in Figure 2a. All measurements are done in ambient conditions.

γ-Ray Detector Measurements. A Kiethley 6487 Picoammeter/voltage source is used to apply the bias voltage. The output signal is amplified with a ORTEC 142PC charge sensitive preamplifier followed by further amplification and filtering by a SR530 amplifier. A Tektronix DPO4104 oscilloscope is used to record the transient signals and a Pixie-Net multichannel digital pulse processor for pulse collection and processing. Radioactive sources used are 49 μCi ^{241}Am, 45 μCi ^{133}Ba, and 226 μCi ^{137}Cs.

ASSOCIATED CONTENT

Supporting Information

The Supporting Information is available free of charge at https://pubs.acs.org/doi/10.1021/acsami.0c11805.

Optical microscope image of the $MAPbI_3$ single-crystal sample; line scans of photocurrent maps for devices with Au−Au and Au−Pb electrodes in absolute scale; photocurrent map and line scans of devices with Au−Pb contacts; photocurrent line scan for a device with Au−Au contacts at 0.5 V bias measured as the laser spot was moved from left to right, right to left, and left to right for a second time in the end; laser intensity dependence of photocurrent profiles; photoemission yield spectroscopy data; pulse rise time for devices with Au−Pb and Au−Au contacts; and schematic of the energy band diagram of Au/$MAPbI_3$/Pb (PDF)

https://dx.doi.org/10.1021/acsami.0c11805
ACS Appl. Mater. Interfaces 2020, 12, 45533−45540

AUTHOR INFORMATION

Corresponding Author

Wanyi Nie − *MPA-11 and CINT, Los Alamos National Laboratory, Los Alamos, New Mexico 87545, United States;* orcid.org/0000-0002-5909-3155; Email: wanyi@lanl.gov

Authors

Shreetu Shrestha − *MPA-11, Los Alamos National Laboratory, Los Alamos, New Mexico 87545, United States;* orcid.org/0000-0002-3606-7624

Hsinhan Tsai − *MPA-11, Los Alamos National Laboratory, Los Alamos, New Mexico 87545, United States*

Michael Yoho − *NEN-1, Los Alamos National Laboratory, Los Alamos, New Mexico 87545, United States*

Dibyajyoti Ghosh − *Theoretical Chemistry and Molecular Physics Division, Los Alamos National Laboratory, Los Alamos, New Mexico 87545, United States;* orcid.org/0000-0002-3640-7537

Fangze Liu − *MPA-11, Los Alamos National Laboratory, Los Alamos, New Mexico 87545, United States*

Yusheng Lei − *University of California, San Diego, La Jolla, California 92121, United States*

Jeremy Tisdale − *MPA-11, Los Alamos National Laboratory, Los Alamos, New Mexico 87545, United States*

Jon Baldwin − *MPA-11 and CINT, Los Alamos National Laboratory, Los Alamos, New Mexico 87545, United States*

Sheng Xu − *University of California, San Diego, La Jolla, California 92121, United States*

Amanda J. Neukirch − *Theoretical Chemistry and Molecular Physics Division, Los Alamos National Laboratory, Los Alamos, New Mexico 87545, United States;* orcid.org/0000-0002-6583-0086

Sergei Tretiak − *Theoretical Chemistry and Molecular Physics Division, Los Alamos National Laboratory, Los Alamos, New Mexico 87545, United States;* orcid.org/0000-0001-5547-3647

Duc Vo − *NEN-1, Los Alamos National Laboratory, Los Alamos, New Mexico 87545, United States*

Complete contact information is available at: https://pubs.acs.org/10.1021/acsami.0c11805

Author Contributions

S.S. fabricated the single-crystal device, carried out the scanning photocurrent microscopy measurements, and wrote the full draft of this manuscript. H.T. grew single crystals and performed structure characterizations for this work. M.Y. built the γ-ray detector setup and analyzed the pulse data. D.G. built the theoretical model for the perovskite surface. F.L. helped on detector measurement. Y.L. grew perovskite single crystal and performed XPS measurement for this work. J.T. contributed to the manuscript writing. J.B. deposited gold metal contacts on the single-crystal device. S.X. involved in data analysis and manuscript writing. A.J.N. involved in theoretical modeling and data interpretation. S.T. supervised D.G. and A.J.N. on the theoretical modeling and interpreted the data. D.V. supervised M.Y. on detector measurements and pulse analysis. W.N. designed the experiment, supervised the project, and wrote the full draft of this manuscript.

Funding

Los Alamos National Laboratory, Laboratory Directed Research and Development (LDRD) program (20180026DR).

Notes

The authors declare no competing financial interest.

ACKNOWLEDGMENTS

This work was supported by the Los Alamos National Laboratory (LANL), Laboratory Directed Research and Development (LDRD) program. This work was conducted, in part, at the Center for Nonlinear Studies (CNLS) and the Center for Integrated Nanotechnologies (CINT), an Office of Science User Facility at LANL operated for the U.S. Department of Energy (DOE) Office of Science. This research used resources provided by the LANL Institutional Computing (IC) Program. LANL is operated by Triad National Security, LLC, for the National Nuclear Security Administration of the U.S. Department of Energy (Contract No. 89233218NCA000001).

REFERENCES

(1) Heo, J. H.; Im, S. H.; Noh, J. H.; Mandal, T. N.; Lim, C.-S.; Chang, J. A.; Lee, Y. H.; Kim, H.-j.; Sarkar, A.; Nazeeruddin, M. K.; Grätzel, M.; Seok, S. I. Efficient Inorganic−Organic Hybrid Heterojunction Solar Cells Containing Perovskite Compound and Polymeric Hole Conductors. *Nat. Photonics* **2013**, *7*, 486−491.

(2) Seok, S. I.; Gratzel, M.; Park, N. G. Methodologies Toward Highly Efficient Perovskite Solar Cells. *Small* **2018**, *14*, No. 1704177.

(3) Tan, Z. K.; Moghaddam, R. S.; Lai, M. L.; Docampo, P.; Higler, R.; Deschler, F.; Price, M.; Sadhanala, A.; Pazos, L. M.; Credgington, D.; Hanusch, F.; Bein, T.; Snaith, H. J.; Friend, R. H. Bright Light-Emitting Diodes Based on Organometal Halide Perovskite. *Nat. Nanotechnol.* **2014**, *9*, 687−692.

(4) Wang, J.; Wang, N.; Jin, Y.; Si, J.; Tan, Z. K.; Du, H.; Cheng, L.; Dai, X.; Bai, S.; He, H.; Ye, Z.; Lai, M. L.; Friend, R. H.; Huang, W. Interfacial Control toward Efficient and Low-Voltage Perovskite Light-Emitting Diodes. *Adv. Mater.* **2015**, *27*, 2311−2316.

(5) Xing, G.; Mathews, N.; Lim, S. S.; Yantara, N.; Liu, X.; Sabba, D.; Gratzel, M.; Mhaisalkar, S.; Sum, T. C. Low-Temperature Solution-Processed Wavelength-Tunable Perovskites for Lasing. *Nat. Mater.* **2014**, *13*, 476−480.

(6) Zhu, H.; Fu, Y.; Meng, F.; Wu, X.; Gong, Z.; Ding, Q.; Gustafsson, M. V.; Trinh, M. T.; Jin, S.; Zhu, X. Y. Lead Halide Perovskite Nanowire Lasers with Low Lasing Thresholds and High Quality Factors. *Nat. Mater.* **2015**, *14*, 636−642.

(7) Stoumpos, C. C.; Malliakas, C. D.; Peters, J. A.; Liu, Z.; Sebastian, M.; Im, J.; Chasapis, T. C.; Wibowo, A. C.; Chung, D. Y.; Freeman, A. J.; Wessels, B. W.; Kanatzidis, M. G. Crystal Growth of the Perovskite Semiconductor $CsPbBr_3$: A New Material for High-Energy Radiation Detection. *Cryst. Growth Des.* **2013**, *13*, 2722−2727.

(8) Fang, Y.; Dong, Q.; Shao, Y.; Yuan, Y.; Huang, J. Highly Narrowband Perovskite Single-Crystal Photodetectors Enabled by Surface-Charge Recombination. *Nat. Photonics* **2015**, *9*, 679−686.

(9) Náfrádi, B.; Náfrádi, G.; Forró, L.; Horváth, E. Methylammonium Lead Iodide for Efficient X-Ray Energy Conversion. *J. Phys. Chem. C* **2015**, *119*, 25204−25208.

(10) Yakunin, S.; Sytnyk, M.; Kriegner, D.; Shrestha, S.; Richter, M.; Matt, G. J.; Azimi, H.; Brabec, C. J.; Stangl, J.; Kovalenko, M. V.; Heiss, W. Detection of X-Ray Photons by Solution-Processed Organic-Inorganic Perovskites. *Nat Photonics* **2015**, *9*, 444−449.

(11) Wei, H.; Fang, Y.; Mulligan, P.; Chuirazzi, W.; Fang, H.-H.; Wang, C.; Ecker, B. R.; Gao, Y.; Loi, M. A.; Cao, L.; Huang, J. Sensitive X-Ray Detectors Made of Methylammonium Lead Tribromide Perovskite Single Crystals. *Nat. Photonics* **2016**, *10*, 333−339.

(12) Ahmadi, M.; Wu, T.; Hu, B. A Review on Organic-Inorganic Halide Perovskite Photodetectors: Device Engineering and Fundamental Physics. *Adv. Mater.* **2017**, *29*, No. 1605242.

(13) Pan, W.; Wu, H.; Luo, J.; Deng, Z.; Ge, C.; Chen, C.; Jiang, X.; Yin, W.-J.; Niu, G.; Zhu, L.; Yin, L.; Zhou, Y.; Xie, Q.; Ke, X.; Sui, M.;

Tang, J. $Cs_2AgBiBr_6$ Single-Crystal X-Ray Detectors with a Low Detection Limit. *Nat. Photonics* **2017**, *11*, 726−732.
(14) Shrestha, S.; Fischer, R.; Matt, G. J.; Feldner, P.; Michel, T.; Osvet, A.; Levchuk, I.; Merle, B.; Golkar, S.; Chen, H.; Tedde, S. F.; Schmidt, O.; Hock, R.; Rührig, M.; Göken, M.; Heiss, W.; Anton, G.; Brabec, C. J. High-Performance Direct Conversion X-Ray Detectors Based on Sintered Hybrid Lead Triiodide Perovskite Wafers. *Nat. Photonics* **2017**, *11*, 436−440.
(15) Wei, W.; Zhang, Y.; Xu, Q.; Wei, H.; Fang, Y.; Wang, Q.; Deng, Y.; Li, T.; Gruverman, A.; Cao, L.; Huang, J. Monolithic Integration of Hybrid Perovskite Single Crystals with Heterogenous Substrate for Highly Sensitive X-Ray Imaging. *Nat. Photonics* **2017**, *11*, 315−321.
(16) Kim, Y. C.; Kim, K. H.; Son, D. Y.; Jeong, D. N.; Seo, J. Y.; Choi, Y. S.; Han, I. T.; Lee, S. Y.; Park, N. G. Printable Organometallic Perovskite Enables Large-Area, Low-Dose X-Ray Imaging. *Nature* **2017**, *550*, 87−91.
(17) Tsai, H.; Liu, F.; Shrestha, S.; Fernando, K.; Tretiak, S.; Scott, B.; Vo, D. T.; Strzalka, J.; Nie, W. A Sensitive and Robust Thin-Film X-Ray Detector Using 2D Layered Perovskite Diodes. *Sci. Adv.* **2020**, *6*, No. eaay0815.
(18) Xu, Z.; Yu, Y.; Arya, S.; Niaz, I. A.; Chen, Y.; Lei, Y.; Miah, M. A. R.; Zhou, J.; Zhang, A. C.; Yan, L.; Xu, S.; Nomura, K.; Lo, Y. H. Frequency- and Power-Dependent Photoresponse of a Perovskite Photodetector Down to the Single-Photon Level. *Nano Lett.* **2020**, *20*, 2144−2151.
(19) Yakunin, S.; Dirin, D. N.; Shynkarenko, Y.; Morad, V.; Cherniukh, I.; Nazarenko, O.; Kreil, D.; Nauser, T.; Kovalenko, M. V. Detection of Gamma Photons Using Solution-Grown Single Crystals of Hybrid Lead Halide Perovskites. *Nat. Photonics* **2016**, *10*, 585−589.
(20) Dirin, D. N.; Cherniukh, I.; Yakunin, S.; Shynkarenko, Y.; Kovalenko, M. V. Solution-Grown $CsPbBr_3$ Perovskite Single Crystals for Photon Detection. *Chem. Mater.* **2016**, *28*, 8470−8474.
(21) Wei, H.; DeSantis, D.; Wei, W.; Deng, Y.; Guo, D.; Savenije, T. J.; Cao, L.; Huang, J. Dopant Compensation in Alloyed $CH_3NH_3PbBr_{3-x}Cl_x$ Perovskite Single Crystals for Gamma-Ray Spectroscopy. *Nat. Mater.* **2017**, *16*, 826−833.
(22) Nazarenko, O.; Yakunin, S.; Morad, V.; Cherniukh, I.; Kovalenko, M. V. Single Crystals of Caesium Formamidinium Lead Halide Perovskites: Solution Growth and Gamma Dosimetry. *NPG Asia Mater.* **2017**, *9*, e373.
(23) He, Y.; Ke, W.; Alexander, G. C. B.; McCall, K. M.; Chica, D. G.; Liu, Z.; Hadar, I.; Stoumpos, C. C.; Wessels, B. W.; Kanatzidis, M. G. Resolving the Energy of Γ-Ray Photons with $MAPbI_3$ Single Crystals. *ACS Photonics* **2018**, *5*, 4132−4138.
(24) He, Y.; Matei, L.; Jung, H. J.; McCall, K. M.; Chen, M.; Stoumpos, C. C.; Liu, Z.; Peters, J. A.; Chung, D. Y.; Wessels, B. W.; Wasielewski, M. R.; Dravid, V. P.; Burger, A.; Kanatzidis, M. G. High Spectral Resolution of Gamma-Rays at Room Temperature by Perovskite $CsPbBr_3$ Single Crystals. *Nat. Commun.* **2018**, *9*, No. 1609.
(25) Tisdale, J. T.; Yoho, M.; Tsai, H.; Shrestha, S.; Fernando, K.; Baldwin, J. K.; Tretiak, S.; Vo, D.; Nie, W. Methylammonium Lead Tribromide Single Crystal Detectors Towards Robust Gamma-Ray Photon Sensing. *Adv. Optical Mater.* **2020**, *8*, No. 2000233.
(26) Liu, F.; Yoho, M.; Tsai, H.; Fernando, K.; Tisdale, J.; Shrestha, S.; Baldwin, J. K.; Mohite, A. D.; Tretiak, S.; Vo, D. T.; Nie, W. The Working Principle of Hybrid Perovskite Gamma-Ray Photon Counter. *Mater. Today* **2020**, *37*, 27−34.
(27) Pan, L.; Feng, Y.; Kandlakunta, P.; Huang, J.; Cao, L. R. Performance of Perovskite $CsPbBr_3$ Single Crystal Detector for Gamma-Ray Detection. *IEEE Trans. Nucl. Sci.* **2020**, *67*, 443−449.
(28) Best Research-Cell Efficiency Chart. https://www.nrel.gov/pv/cell-efficiency.html (accessed March 02).
(29) Béchu, S.; Ralaiarisoa, M.; Etcheberry, A.; Schulz, P. Photoemission Spectroscopy Characterization of Halide Perovskites. *Adv. Energy Mater.* **2020**, *10*, No. 1904007.
(30) Huang, L.; Zhang, D.; Bu, S.; Peng, R.; Wei, Q.; Ge, Z. Synergistic Interface Energy Band Alignment Optimization and Defect Passivation toward Efficient and Simple-Structured Perovskite Solar Cell. *Adv. Sci.* **2020**, *7*, No. 1902656.
(31) Kanda, H.; Shibayama, N.; Huckaba, A. J.; Lee, Y.; Paek, S.; Klipfel, N.; Roldán-Carmona, C.; Queloz, V. I. E.; Grancini, G.; Zhang, Y.; Abuhelaiqa, M.; Cho, K. T.; Li, M.; Mensi, M. D.; Kinge, S.; Nazeeruddin, M. K. Band-Bending Induced Passivation: High Performance and Stable Perovskite Solar Cells Using a Perhydropoly-(Silazane) Precursor. *Energy Environ. Sci.* **2020**, *13*, 1222−1230.
(32) Dänekamp, B.; Muller, C.; Sendner, M.; Boix, P. P.; Sessolo, M.; Lovrincic, R.; Bolink, H. J. Perovskite-Perovskite Homojunctions Via Compositional Doping. *J. Phys. Chem. Lett.* **2018**, *9*, 2770−2775.
(33) Ahn, Y.; Dunning, J.; Park, J. Scanning Photocurrent Imaging and Electronic Band Studies in Silicon Nanowire Field Effect Transistors. *Nano Lett.* **2005**, *5*, 1367−1370.
(34) Graham, R.; Miller, C.; Oh, E.; Yu, D. Electric Field Dependent Photocurrent Decay Length in Single Lead Sulfide Nanowire Field Effect Transistors. *Nano Lett.* **2011**, *11*, 717−722.
(35) Gu, Y.; Romankiewicz, J. P.; David, J. K.; Lensch, J. L.; Lauhon, L. J.; Kwak, E. S.; Odom, T. W. Local Photocurrent Mapping as a Probe of Contact Effects and Charge Carrier Transport in Semiconductor Nanowire Devices. *J. Vac. Sci. Technol., B* **2006**, *24*, 2172.
(36) Kelzenberg, M. D.; Turner-Evans, D. B.; Kayes, B. M.; Filler, M. A.; Putnam, M. C.; Lewis, N. S.; Atwater, H. A. Photovoltaic Measurements in Single-Nanowire Silicon Solar Cells. *Nano Lett.* **2008**, *8*, 710−714.
(37) Son, B. H.; Park, J. K.; Hong, J. T.; Park, J. Y.; Lee, S.; Ahn, Y. H. Imaging Ultrafast Carrier Transport in Nanoscale Field-Effect Transistors. *ACS Nano* **2014**, *8*, 11361−11368.
(38) Soudi, A.; Dhakal, P.; Gu, Y. Diameter Dependence of the Minority Carrier Diffusion Length in Individual Zno Nanowires. *Appl. Phys. Lett.* **2010**, *96*, No. 253115.
(39) Wu, C.-C.; Jariwala, D.; Sangwan, V. K.; Marks, T. J.; Hersam, M. C.; Lauhon, L. J. Elucidating the Photoresponse of Ultrathin Mos2 Field-Effect Transistors by Scanning Photocurrent Microscopy. *J. Phys. Chem. Lett.* **2013**, *4*, 2508−2513.
(40) Strasfeld, D. B.; Dorn, A.; Wanger, D. D.; Bawendi, M. G. Imaging Schottky Barriers and Ohmic Contacts in PbS Quantum Dot Devices. *Nano Lett.* **2012**, *12*, 569−575.
(41) Semonin, O. E.; Elbaz, G. A.; Straus, D. B.; Hull, T. D.; Paley, D. W.; van der Zande, A. M.; Hone, J. C.; Kymissis, I.; Kagan, C. R.; Roy, X.; Owen, J. S. Limits of Carrier Diffusion in N-Type and P-Type $CH_3NH_3PbI_3$ Perovskite Single Crystals. *J. Phys. Chem. Lett.* **2016**, *7*, 3510−3518.
(42) Liu, S.; Wang, L.; Lin, W. C.; Sucharitakul, S.; Burda, C.; Gao, X. P. Imaging the Long Transport Lengths of Photo-Generated Carriers in Oriented Perovskite Films. *Nano Lett.* **2016**, *16*, 7925−7929.
(43) Xiao, R.; Hou, Y.; Fu, Y.; Peng, X.; Wang, Q.; Gonzalez, E.; Jin, S.; Yu, D. Photocurrent Mapping in Single-Crystal Methylammonium Lead Iodide Perovskite Nanostructures. *Nano Lett.* **2016**, *16*, 7710−7717.
(44) Wang, X.; Ling, Y.; Chiu, Y. C.; Du, Y.; Barreda, J. L.; Perez-Orive, F.; Ma, B.; Xiong, P.; Gao, H. Dynamic Electronic Junctions in Organic-Inorganic Hybrid Perovskites. *Nano Lett.* **2017**, *17*, 4831−4839.
(45) Herz, L. M. Charge-Carrier Mobilities in Metal Halide Perovskites: Fundamental Mechanisms and Limits. *ACS Energy Lett.* **2017**, *2*, 1539−1548.
(46) Dong, Q.; Fang, Y.; Shao, Y.; Mulligan, P.; Qiu, J.; Cao, L.; Huang, J. Solar Cells. Electron-Hole Diffusion Lengths> 175 μm in Solution-Grown $CH_3NH_3PbI_3$ Single Crystals. *Science* **2015**, *347*, 967−970.
(47) Zu, F.; Wolff, C. M.; Ralaiarisoa, M.; Amsalem, P.; Neher, D.; Koch, N. Unraveling the Electronic Properties of Lead Halide Perovskites with Surface Photovoltage in Photoemission Studies. *ACS Appl. Mater. Interfaces* **2019**, *11*, 21578−21583.
(48) Haruyama, J.; Sodeyama, K.; Han, L.; Tateyama, Y. Termination Dependence of Tetragonal $CH_3NH_3PbI_3$ Surfaces for Perovskite Solar Cells. *J. Phys. Chem. Lett.* **2014**, *5*, 2903−2909.

https://dx.doi.org/10.1021/acsami.0c11805
ACS Appl. Mater. Interfaces 2020, 12, 45533−45540

(49) Quarti, C.; De Angelis, F.; Beljonne, D. Influence of Surface Termination on the Energy Level Alignment at the $CH_3NH_3PbI_3$ Perovskite/C60 Interface. *Chem. Mater.* **2017**, *29*, 958−968.
(50) She, L.; Liu, M.; Zhong, D. Atomic Structures of $CH_3NH_3PbI_3$ (001) Surfaces. *ACS Nano* **2016**, *10*, 1126−1131.
(51) Ohmann, R.; Ono, L. K.; Kim, H. S.; Lin, H.; Lee, M. V.; Li, Y.; Park, N. G.; Qi, Y. Real-Space Imaging of the Atomic Structure of Organic-Inorganic Perovskite. *J. Am. Chem. Soc.* **2015**, *137*, 16049−16054.
(52) Uratani, H.; Yamashita, K. Charge Carrier Trapping at Surface Defects of Perovskite Solar Cell Absorbers: A First-Principles Study. *J. Phys. Chem. Lett.* **2017**, *8*, 742−746.
(53) Meggiolaro, D.; De Angelis, F. First-Principles Modeling of Defects in Lead Halide Perovskites: Best Practices and Open Issues. *ACS Energy Lett.* **2018**, *3*, 2206−2222.
(54) Fu, D.; Zou, J.; Wang, K.; Zhang, R.; Yu, D.; Wu, J. Electrothermal Dynamics of Semiconductor Nanowires under Local Carrier Modulation. *Nano Lett.* **2011**, *11*, 3809−3815.
(55) Kedem, N.; Kulbak, M.; Brenner, T. M.; Hodes, G.; Cahen, D. Type-Inversion as a Working Mechanism of High Voltage $MAPbBr_3$(Cl)-Based Halide Perovskite Solar Cells. *Phys. Chem. Chem. Phys.* **2017**, *19*, 5753−5762.
(56) Shi, D.; Adinolfi, V.; Comin, R.; Yuan, M.; Alarousu, E.; Buin, A.; Chen, Y.; Hoogland, S.; Rothenberger, A.; Katsiev, K.; Losovyj, Y.; Zhang, X.; Dowben, P. A.; Mohammed, O. F.; Sargent, E. H.; Bakr, O. M. Solar Cells. Low Trap-State Density and Long Carrier Diffusion in Organolead Trihalide Perovskite Single Crystals. *Science* **2015**, *347*, 519−522.
(57) Saidaminov, M. I.; Abdelhady, A. L.; Murali, B.; Alarousu, E.; Burlakov, V. M.; Peng, W.; Dursun, I.; Wang, L.; He, Y.; Maculan, G.; Goriely, A.; Wu, T.; Mohammed, O. F.; Bakr, O. M. High-Quality Bulk Hybrid Perovskite Single Crystals within Minutes by Inverse Temperature Crystallization. *Nat. Commun.* **2015**, *6*, No. 7586.
(58) Liu, Y.; Yang, Z.; Cui, D.; Ren, X.; Sun, J.; Liu, X.; Zhang, J.; Wei, Q.; Fan, H.; Yu, F.; Zhang, X.; Zhao, C.; Liu, S. F. Two-Inch-Sized Perovskite $CH_3NH_3PbI_3$(X = Cl, Br, I) Crystals: Growth and Characterization. *Adv. Mater.* **2015**, *27*, 5176−5183.

https://dx.doi.org/10.1021/acsami.0c11805
ACS Appl. Mater. Interfaces 2020, 12, 45533−45540